Physica Medica 65 (2019) 114–120

Contents lists available at ScienceDirect

Physica Medica

journal homepage: www.elsevier.com/locate/ejmp

Original paper

Characterization of scintillating fibers for use as positron detector in positron emission tomography

Vincent Turgeon[a,b,*], Gustavo Kertzscher[c], Liam Carroll[a], Robert Hopewell[d], Gassan Massarweh[d], Shirin A. Enger[a,e,f]

[a] Medical Physics Unit, McGill University, Montreal, Quebec, Canada
[b] Jewish General Hospital, Montreal, Quebec, Canada
[c] Aarhus University Hospital, Aarhus, Denmark
[d] Montreal Neurological Institute and Hospital, Montreal, Quebec, Canada
[e] Department of Oncology, McGill University, Montreal, Quebec, Canada
[f] Research Institute of the McGill University Health Centre, Montreal, Quebec, Canada

ARTICLE INFO

Keywords:
Scintillating fibers
Arterial input function
Radiation detector
Dynamic PET

ABSTRACT

Purpose: Manual and automatic blood sampling at different time intervals is considered the gold standard to determine the arterial input function (AIF) in dynamic positron emission tomography (PET). However, blood sampling is characterized by poor time resolution and is an invasive procedure. The aim of this study was to characterize the scintillating fibers used to develop a non-invasive positron detector.

Methods: The detector consists of a scintillating fiber coupled at each end to transmission fiber-optic cables that are connected to photo multiplier tubes in a dual readout setup. The detector is designed to be wrapped around the wrist of the patient undergoing dynamic PET. The attenuation length and bending losses were measured with excitation from gamma radiation (^{137}Cs) and ultraviolet (UV) light. The response to positron-emitting radiotracers was evaluated with ^{18}F and ^{11}C.

Results: The attenuation length for a 3.0 m and 1.5 m long scintillating fiber both coincides with the attenuation length given by the manufacturer when excited with the ^{137}Cs source, but not with the UV source due to the differences in scintillation mechanisms. The bending losses are smaller than the measurement uncertainty for the ^{137}Cs source irradiation, and increase when the bending radius decrease for the UV source irradiation. The signal-to-noise ratio for ^{18}F and ^{11}C solutions are 1.98 and 22.54 respectively. The measured decay constant of ^{11}C agrees with its characteristic value.

Conclusion: The performed measurements in the dual readout configuration suggest that scintillating fibers may be suitable to determine the AIF non-invasively.

1. Introduction

Quantitative information on metabolic processes is often obtained through kinetic modeling of dynamic positron emission tomography (PET) images. A solution of radiotracers is injected in the patient's blood vessels and several images are acquired at different time frames to record the radiotracers concentration as a function of time. Kinetic modeling requires knowledge of the radioactivity concentration in the arteries, known as the arterial input function (AIF) [1]. Currently, invasive manual or automatic blood sampling at different time intervals during the scan is considered the gold standard to determine the AIF. However, the limited time resolution of this process prevents the accurate determination of the peak-value of the AIF, and its invasiveness causes discomfort to the patient. In addition, manual or automatic blood sampling requires highly trained personnel to perform the procedure and additional laboratory space and equipment to analyze the blood samples, which limit the use of kinetic modeling to academic PET centers with adequate financial and technical resources.

Previous studies have investigated different types of radiation detectors to measure the AIF non-invasively, including scintillation detectors based on solid organic plastics or inorganic crystals as well as a miniature PET scanner to image the wrist [2–7]. None of the proposed detectors was widely disseminated to PET centers due to the high cost and the low signal-to-noise ratio (SNR) owing to detection of background radiation from the patient's body. As an alternative, we propose a new non-invasive and cost-effective radiation detector based on

* Corresponding author at: Medical Physics Unit, McGill University, Montreal, Quebec, Canada.
E-mail address: vincent.turgeon@mail.mcgill.com (V. Turgeon).

https://doi.org/10.1016/j.ejmp.2019.08.009
Received 14 May 2019; Received in revised form 15 July 2019; Accepted 11 August 2019
Available online 23 August 2019

plastic scintillating fibers placed on the wrist of the patient in circular loops similar to bracelets, and subsequently measure the AIF through detection of emitted positrons passing through the radial and ulnar arteries. The wrist was selected due to the closeness of the arteries to the skin surface. The maximum range of positrons in soft tissue emitted from radionuclides used in PET is between 2.6 and 10 mm [8] and the average depth of the arteries in the wrist is 1.99 ± 0.99 mm [9].

Scintillating fibers are currently used as survey meters in nuclear reactors [10], as calorimeters in high energy physics [11] and as dosimeters in cancer treatment with radiation therapy [12]. Dopants added in the core of the fibers act as scintillation light emitters. When ionizing radiation deposits energy in the scintillating fiber, the dopant molecules are brought to an excited energy level. The molecules return to the ground energy level by emitting photons with frequencies corresponding to the difference in energy between the excited and the ground energy level [13]. The dopants are selected so that the difference in energy corresponds to visible wavelengths. The scintillation photons are emitted isotropically. The photons that are emitted within the critical angle of the scintillating fiber are transmitted through the fiber toward a light detection device at the end of the fiber. The total number of photons detected with the light detection device will depend on the quantum efficiency of the light detection device, the coupling efficiency between the light detection device and the scintillating fiber, the fraction of scintillating photons that are trapped by total internal reflection in the scintillating fiber and finally, on the attenuation of the signal inside the scintillating fiber [14,12]. The aim of the current study was to characterize the scintillating fiber used in the development of a non-invasive positron detector to monitor the AIF. Since the scintillating fiber was bent to be wrapped around the patient's wrist, the losses of signal due to bending of the fiber was measured in addition to measurements of the attenuation length of the scintillating fiber. Furthermore, since positrons emitted from commonly used PET radionuclides have different range in tissue, measurements with two different PET radionuclides were performed to investigate the difference in signal due to varying range of positrons. Detector response to different radioactivity levels was also studied.

2. Materials and methods

2.1. Detector setup

The detector consists of a scintillating fiber with a core of polystyrene (BCF-12, Saint-Gobain Crystals and Detectors, Paris, France) optically coupled at each end to 11 meters of transmission fiber with a core of PMMA (Eska-GH4001, Mitsubishi Chemical, Japan). The scintillating fiber is covered by a 7.2 μm thick black tubing (Vention Medical, USA) to provide mechanical robustness. Each end of the transmission fibers is connected to a photomultiplier tube (PMT) (H6779, Hamamatsu, Japan). The output waveforms from the PMTs are monitored simultaneously with an oscilloscope (DSO-X 2012A, Keysight, USA) without amplification. Fig. 1 is a representation of the prototype dual readout setup. Table 1 lists several properties of the scintillating and transmission fibers. The oscilloscope signal is recorded with a Matlab (R2017a) script.

2.2. Attenuation measurements

Since the emission and absorption spectra of plastic scintillating fibers overlap [13], it is necessary to measure the attenuation of the light signal as a function of distance traveled in the scintillating fiber. In this study, a dual readout setup with two different detector configurations was tested. The first detector was built with 1.5 m scintillating fiber and the second detector with 3.0 m scintillating fiber. A ^{137}Cs gamma source with the activity of 186.5 kBq and a radius of 2.5 cm was positioned each 10 cm along the fibers. In total, there were 15 and 29 points of measurements for the 1.5 m and 3.0 m scintillating fiber

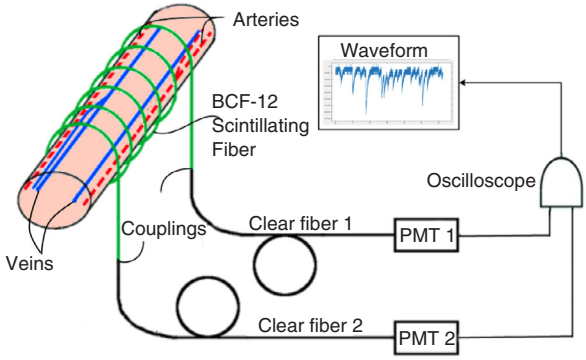

Fig. 1. Schematic representation of the dual readout detector.

Table 1
Properties of scintillating and transmission fibers. Data obtained from the Saint-Gobain and ESKA.

Characteristic	BCF-12	Eska GH4001
Core material	Polystyrene	PMMA
Core density	1.05 g/cm^3	1.2 g/cm^3
Core refractive index	1.60	1.49
Cladding material	PMMA	Fluorinated Polymer
Cladding refractive index	1.49	N/A
Diameter, with cladding	1.00 ± 0.02 mm	1.000 mm
Numerical aperture	0.74	0.5
1/e attenuation length	270 cm	5101 cm
Emission peak	435 nm	–
Scintillation decay time	3.2 ns	–
# of photons/ MeV	≈8000	–

respectively. Fig. 2-A represents a schematic of the setup with the 3.0 m scintillating fiber. The gain of each PMT needed to be adjusted to obtain approximately an equal output for an excitation at the center position on the scintillating fiber. For each position of the source, ten 5 ms output waveforms from the PMTs with a sampling rate of 12.5 MHz were acquired using the oscilloscope. Each waveform was integrated, and the ten individual sums were averaged. An example of the waveform is displayed on Fig. 2-B. To account for the background level, ten measurements without the source were made and the average background level subtracted to the signal. The attenuation of the signal follows an exponential function [13]:

$$S = A \cdot e^{-d/\lambda_a} \quad (1)$$

where S is the integrated signal from the PMT, d is the distance between the excitation point and the PMT, λ_a is the 1/e attenuation length of the scintillating fiber and A is a normalization constant. In this study, the ratio of the output at each PMT (S_1/S_2) was used and the ratio theoretically follows a decreasing mono exponential function with the form:

$$\frac{S_1}{S_2} = e^{-2x/\lambda_a} \quad (2)$$

where S_1 and S_2 are the integrated signals from the first and the second PMT respectively, and x is the distance between the source and the PMT, defined as $x = 0$ at the center of the fiber. This ratio was normalized to 1 when the excitation source was at the center of the fiber. Since the scintillation light generated by the ^{137}Cs source is weak, the same measurements were performed with a UV lamp (36 W), which produced a much larger and sufficiently constant light signal.

2.3. Bending losses

As shown in Fig. 1, the scintillating fiber is wrapped around the patient's wrist to increase the detection area. Bending the fiber can change its shape and therefore reduce the detector efficiency [15]. To

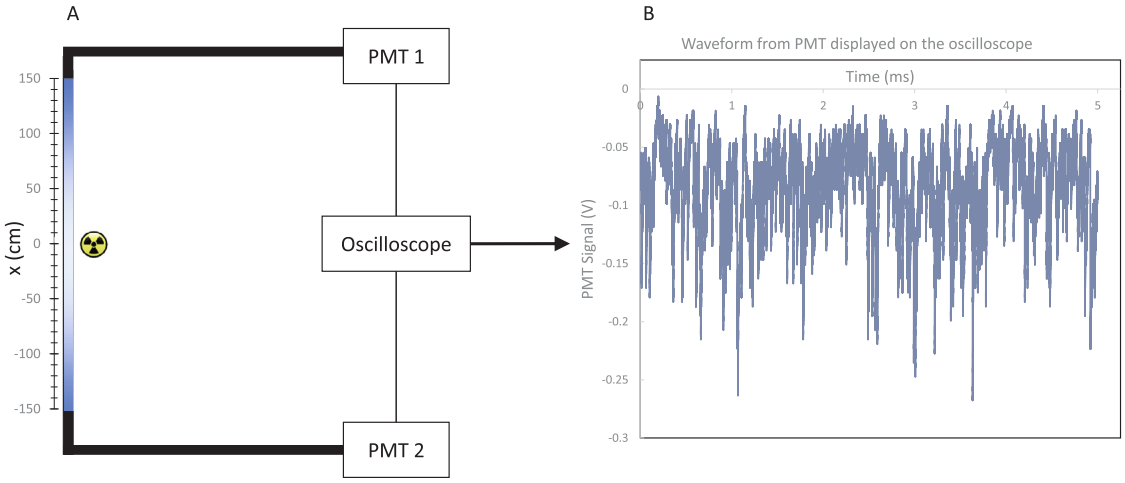

Fig. 2. Schematic of the attenuation measurement setup. A: Disposition of the radioactive source along the scintillating fiber. The scintillating fiber is connected at both ends to a transmission fiber. Each transmission fiber is connected to a PMT. The PMTs' signal is recorded by the oscilloscope. B: Waveform that is outputed by the PMTs. The oscilloscope records a 5 ms train of voltage pulses from the PMTs. The integration of this waveform is used as S in Eqs. (1) and (2).

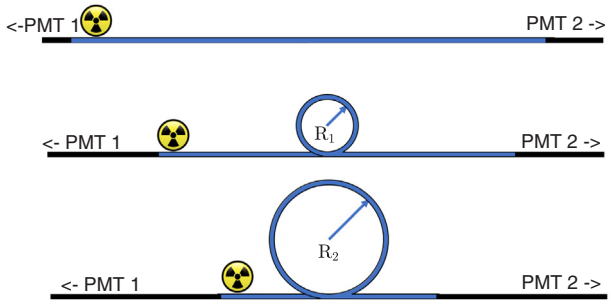

Fig. 3. Setup for the bending loss measurement. The total length of the scintillating fiber (blue) was constant for each loop. The position of the excitation source was also kept constant. (For interpretation of the references to colour in this figure legend, the reader is referred to the web version of this article.)

evaluate this, the difference in output at each PMT was measured for a fixed excitation point at one end of the scintillating fiber and different loop diameters in the fiber, as shown in Fig. 3. Due to the finite length of the scintillating fiber and to make sure that the excitation source did not generate scintillation in the bent portion of the fiber, there was only one loop for each measurement. The signal was acquired in the same way as described in the previous section. The measurements were also performed with the UV source. The losses L were calculated as:

$$L = \frac{R_0 - R_y}{R_0} \cdot 100 \quad (3)$$

Where R_0 is the ratio between the outputs of PMT_2 and PMT_1 when the fiber is straight and R_y is the same ratio for different bending radii y of the scintillating fiber.

2.4. Positron measurements

The signal detected by the detector depends on the amount of positrons reaching the scintillating fiber. The two radionuclides available for this study were ^{18}F and ^{11}C. The radionuclides' half-life, maximum and mean positron energy and range in water are displayed in Table 2. ^{18}F emits positrons with the lowest range in tissue but is the most commonly used radionuclide in PET. The longer range of positrons emitted from ^{11}C makes it a much better candidate to be used in combination with the purposed detector. To evaluate the difference in

Table 2
Half-life, mean and maximum values for energy and range in water of ^{18}F and ^{11}C [8].

Isotopes	Half-life (min)	E_{mean} (keV)	E_{max} (keV)	R_{mean} (mm)	R_{max} (mm)
^{18}F	109.8	252	635	0.66	2.633
^{11}C	20.3	390	970	1.266	4.456

signal based on the range of emitted positrons, a cylindrical polyethylene (density 0.94 g/cm^3) phantom with a diameter of 6.41 cm and length of 6.48 cm was used to mimic the wrist. Holes with a diameter of 3.25 mm situated at a depth of 2 mm were drilled in the phantom to simulate the attenuation from the tissue. The dimensions were verified with transverse MRI images of the wrist. Polyethylene and soft tissue have similar attenuation coefficients for 500 keV photons, with 0.106 cm^{-1} and 0.096 cm^{-1} respectively [16] and similar stopping power for positrons in the range of energies relevant to PET [17]. The scintillating part of the detector was wrapped five times around the phantom with a bending radius of 12 cm.

A 1.5 m long plastic tube was used to pass the radioactive solutions through the phantom and exit into a waste bottle shielded as shown in the Fig. 4. The radioactivity concentration of the solution was measured with a Caprac well counter (Capintec, USA) and was 7.4 ± 0.1 MBq/ml and 3.7 ± 0.1 MBq/ml for ^{18}F and ^{11}C respectively. The radioactive solutions were injected as a pulse inside the phantom. The response of

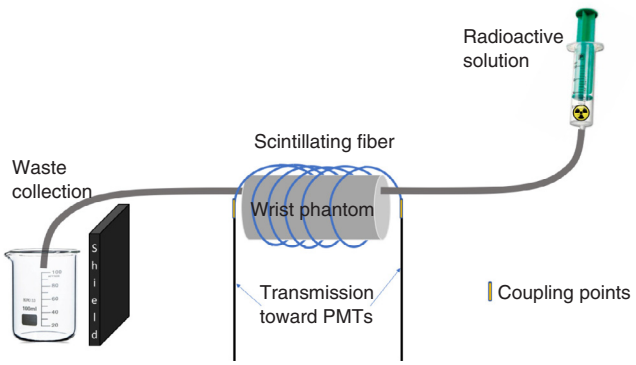

Fig. 4. Representation of the phantom with a tube imitating a blood vessel. The radioactive solution was injected through the tube and collected in a waste recipient shielded from the detector.

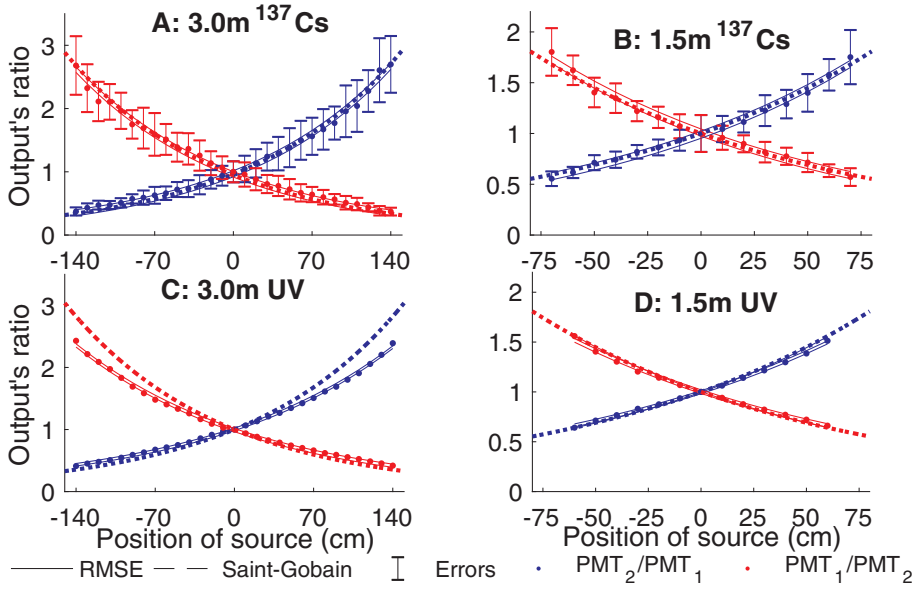

Fig. 5. Attenuation length measurements for the 3.0 m detector, with the ^{137}Cs and the UV sources (A and C respectively). B and D show the attenuation length measurements with the ^{137}Cs and the UV sources, but for the 1.5 m detector.

the detector was monitored with the oscilloscope recording 5 ms waveforms with a rate of 2.87 waveforms per second. The signal from each waveform was integrated over the entire 5 ms. The acquisition for the ^{18}F solution lasted 4 min and 15 s and the ^{11}C lasted 1 min and 56 s. The background level was subtracted from the signal as described previously.

In addition, the response to different levels of radioactivity was measured with the solution of ^{11}C. Its 20.3 min half-life makes it a good candidate to measure its decay over a relatively short period of time. 3.02 MBq of ^{11}C was inserted inside the phantom and a 5 ms waveform was acquired every 1.4 s for a total time of 1 h, 24 min and 31 s. The decay constant for ^{11}C was extracted from an exponential fit of the data with Matlab.

3. Results

3.1. Attenuation measurements

Fig. 5 shows the attenuation length measurements for the 3.0 m detector with the ^{137}Cs (Fig. 5A) and UV source (Fig. 5-C). Fig. 5-B and Fig. 5-D presents the ^{137}Cs and UV source excitations respectively, but for the 1.5 m detector. The ratio PMT_1 over PMT_2 is displayed in red, and the inverse in blue. The filled circles are the average of 10 measurements performed at each position. The vertical lines are the uncertainties for the 10 measurements, calculated using the quadratic sum of the relative uncertainties on each PMT output [18]. The uncertainties do not show on the UV measurements, as they are too small. The dashed curves are exponential curves from Eq. (2) with $\lambda_a = 270$ cm, the attenuation length specified by Saint-Gobain. Finally, the solid curves are the boundaries defined by the root mean square error (RMSE) on the fit of Eq. (2) on the data. The attenuation lengths obtained from the ^{137}Cs measurements are 277 ± 12 cm and 261 ± 16 cm for the 3.0 m and 1.5 m detectors, respectively. With the UV source, the measured attenuation lengths are 307 ± 6 cm and 294 ± 8 cm, for the 3.0 m and 1.5 m detectors, respectively. The uncertainty on the attenuation lengths comes from the 95 % confidence interval from the fitting algorithm.

3.2. Bending losses

The bending losses calculated from Eq. (3) are shown in Table 3. The uncertainty of the bending losses for the ^{137}Cs measurements were larger than the measured losses for every radius. However, with the UV measurements, the uncertainties of the losses percentage are on the order of 0.0002%. The very small uncertainty allows to see that the losses increase linearly as the bending radius decreases.

3.3. Positron measurements

The injection of radioactivity measurements are presented in Fig. 6-A for ^{18}F and Fig. 6-B for ^{11}C. The red curves represent the integrated signal of the 5 ms waveforms acquired with the oscilloscope. The black curves are the moving averages of 5 data points. Both figures are normalized to 100 at the maximum of the smoothed data. The top part of the ^{18}F step function starts after 32 s and the injection lasts 36 s. The top part for the ^{11}C step function rises at the 30 s' mark and the injection lasts 26 s. The SNR was taken by dividing the mean of top part of the step function divided by the standard deviation of the bottom part of the step function [19]. The SNR is 1.98 and 22.54 for the ^{18}F and ^{11}C respectively.

The red curve on Fig. 7 shows the integrated signal from the oscilloscope over 84 min when a solution of ^{11}C is inserted in the phantom. The decay constant extracted from the exponential fit is $(5.63 \pm 0.09)\cdot 10^{-4}$ s^{-1}. The starting point of activity concentration was 3.02 MBq/ml. The uncertainty on the decay constant represents the 95% confidence interval on the fit. The black solid curve on Fig. 7 is the fitted decay curve and the yellow dotted curve is the theoretical decay, normalized to the same value as the fitted curve. The decay constant for ^{11}C is $5.673\cdot 10^{-4}$ s^{-1} [20]. Both curves are in good agreement.

4. Discussion

4.1. Attenuation measurements

An attenuation length of 270 cm is provided by Saint-Gobain for BCF-12 scintillating fiber in their catalog [21], but the attenuation length will vary depending on the experimental setup [22]. On one hand, the attenuation in the scintillating fiber is a function of wavelength of the transmitted light. On the other, light detection devices have different responses to the spectrum of incident light, meaning that the same scintillating fiber can appear to have a different attenuation length if measured with different light detecting device. The

Table 3
Losses (in percent) from Eq. (3) for different bending radii compared to a straight fiber. UV uncertainties ≈ 0.0002%.

	Scintillating fiber bending radius (cm)						
	15.0	13.5	12.0	10.5	9.0	7.5	6.0
UV	0.82	0.87	1.13	1.45	1.59	1.72	2.20
^{137}Cs	3.1 ± 5.4	3.0 ± 6.8	3.4 ± 6.5	4.4 ± 7.8	2.8 ± 6.3	2.1 ± 6.3	4.5 ± 5.7

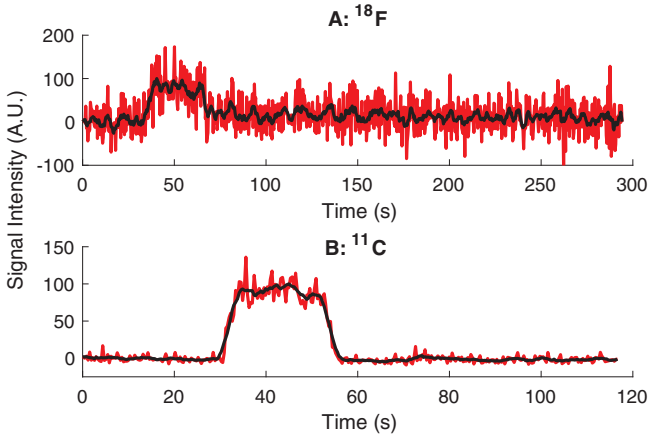

Fig. 6. A: Injection of ^{18}F radioactive solution. B: Injection of ^{11}C radioactive solution. The red lines are the experimental data. The black lines correspond to the moving average of 5 points. (For interpretation of the references to colour in this figure legend, the reader is referred to the web version of this article.)

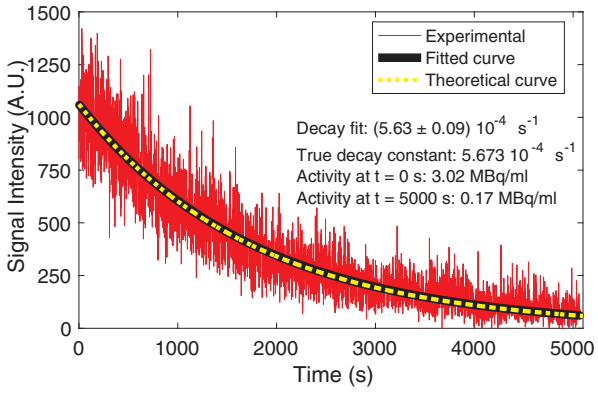

Fig. 7. Decay of ^{11}C measured over 84 min with the proposed detector. The red curve represents the experimental data. The black solid and yellow dotted curves are the mono exponential fit and the theoretical decay, respectively. Both curves are in good agreement.

attenuation length measurements reported by Saint-Gobain were performed with a ^{90}Sr electron source and a motor on a precision track with a 1 mm precision to move the source along a straight 3 m sample of scintillating fiber with a PMT at a single end of the fiber. The company specified that the uncertainty on the measurements is within 5%, corresponding to ± 8 cm for an attenuation length of 270 cm. The attenuation length obtained in this study with the ^{137}Cs source agree with the value from Saint-Gobain, but the results obtained with the UV light do not. Panel C in Fig. 5 shows the divergence of our experimental results from the manufacturer's data. In panel D, the length of the detector is too short to clearly visualize the difference. The attenuation length obtained using the UV source did not agree with the manufacturer's data due to the material composition of the BCF-12 fiber, which consists of polystyrene, a primary dye and a secondary dye. The UV source excites only the secondary dye, while the ionizing radiation first excites the base polymer which then transfers energy to the primary dye. The primary dye emits light that is absorbed by the secondary dye and re-emitted at longer wavelength, with a peak at 435 nm [23]. This situation could be further investigated with a different equation for the attenuation, but since the UV spectrum will be absent in clinical situation, it is beyond the scope of this work. UV measurements will uniquely be used for a rapid verification of light transmission in newly built detectors.

Attenuation length of scintillating fibers have been studied in the past by other groups. Amos et al. [24] and Hawkes et al. [25] investigated the effect of the cladding material on the transmission of light. Both studies concluded that the amount of light transmitted through the cladding is higher than inside the core over the first 50 cm of the scintillating fiber. However, the reflections at the air-cladding interface are poorer than the reflections at the cladding-core interface. It is the core light that dominates at longer distances. Due to the length of the detector investigated in this study, it is the core light that dominates the signal.

4.2. Bending losses

The smallest uncertainty and the largest signal loss due to the bending of the fiber with the ^{137}Cs radiation source are 5.4% and 4.4% respectively. Chung et al. [26] also obtained losses smaller than their measurement uncertainties when investigating bending losses. It is possible to see the relation between the bending radius and the light loss because the UV-lamp generates an intense signal that is 52 times greater than the background signal. In contrast, the smaller signal intensity generated with the Cs-137 source results in uncertainties that are greater than previously reported bending losses.

A previous study reported bending losses in Kuraray scintillating fibers on the order 1% for bending radius of 6 cm and larger losses as the bending radius decreased down to 1 cm [15]. When the authors investigated the losses for multiple loops with a 0.965 mm diameter Kuraray fiber, losses smaller than 2% were observed for 10 loops with a radius of 3.5 cm [15].In the present work, smaller radius are not useful as a human hand needs to be slipped inside the loops for the detector to be used on patients. Chung et al. [26] also concluded that the attenuation length did not change over 3.5 years for Kuraray fibers properly stored. In addition, the bending losses did not change for fibers kept bent for a year in coils with 10 turns and a radius of 3 cm. Finally, the UV lamp was not the ideal choice of excitation for this experiment. The UV-generated photoluminescence along the fiber may vary from bending radius to bending radius if the UV transmission is highly affected by the radii. However, based on the previously mentioned publications and our results, the bending of the scintillating fibers into bracelets will not degrade the transmission of the signal in a clinical scenario.

4.3. Positron measurements

The increase in signal as the solution reaches the phantom can be seen with both radioactive solutions. The slopes on the side of the step function comes from the finite time required to detect the entire solution. The better SNR when measuring ^{11}C can be explained with the longer range of its positrons. The maximum range in tissue of positrons from the ^{11}C decay is 4.456 mm, in contrast to 2.633 mm for the ^{18}F

decay. The increase in SNR confirms that it is easier to detect isotopes emitting positrons of higher energy, and therefore longer range. Positrons emitted from other commonly used radionuclides in PET such as ^{13}N, ^{15}O and ^{68}Ga, have longer maximum range in tissue; 5.752 mm, 9.132 mm and 10.273 mm respectively. Future work will include repeating the phantom measurements with these radionuclides to further investigate the detector sensitivity.

The sampling rate of the oscilloscope was 2.87 data points per second for this experiment. This timing resolution allowed for the distinction of the gradients in signal caused by the radioactive solution entering and exiting the phantom. Previous designs relied on LSO crystals to create an image of radioactive solutions passing through a phantom [27]. Because LSO crystals record counts of 511 keV photons interactions within the crystals, the sampling rate must be long enough to acquire enough count to increase the SNR. A slower sampling rate will result in a lower time resolution and cause the gradient in signal to be less sharp. The time resolution is a crucial parameter, as it is imperative to have a precise definition of the AIF peak in kinetic modeling.

Our detector has an accurate response to varying levels of radioactivity, as demonstrated by accurately measuring the decay constant of $(5.63 \pm 0.09)\cdot 10^{-4} s^{-1}$ (most recent data is $5.673\cdot 10^{-4}\ s^{-1}$ [20]). The final activity concentration for Fig. 7 is 0.17 MBq/ml, and the blood activity concentration in PET studies is around 0.09 MBq/ml [5]. Therefore, the response of the detector needs to be evaluated for activity concentrations even lower than what was used in this study. As oppose to discrete acquisition of signal waveform as it was done in this study, a continuous reading might increase the sensitivity of the detectors. Other alternatives to increase the sensitivity are to use light detection devices with higher gain or efficiency or even to use amplifiers after the light detection device.

Finally, when charged particle travel faster than the speed of light in a medium, they emit light known as Cerenkov radiation [28]. Cerenkov radiation adds an additional signal in the background. With BCF-12, the threshold energy for electrons and positrons to generate Cerenkov radiation is 144 keV [29]. Many studies with optical fibers in the fields of dosimetry and radiation detection have investigated the contribution of Cerenkov radiation [30–34]. These articles concluded that the amount of Cerenkov light produced per unit length of irradiated scintillating fiber is very small compared to the scintillation light signal. The main contribution of Cerenkov comes from the clear transmission fiber, where no scintillation happens. The Cerenkov contribution can be considered negligible if the clear transmission fiber is not directly in the radiation beam's path. In the case of the detector developed in this study, the scintillation signal from undesired gamma rays detected by the scintillating fiber will be the dominant source of noise compared to the Cerenkov signal from the clear transmission fiber.

5. Conclusion

This work describes the characterization of the scintillating fiber used in development of a positron detector prototype for non-invasive measurement of the AIF. The performed measurements in the dual readout configuration suggest that scintillating fibers are suitable for this application.

Acknowledgments

The authors acknowledge support by the Canada Foundation for Innovation Leaders Opportunity Fund (Grant No.: 34987), the Natural Sciences and Engineering Research Council (NSERC) (Grant No.: 241018), the NSERC CREATE Medical Physics Research Training Network (Grant No.: 432290) and the Fond Quebecois de la Recherche sur la Nature et les Technologies (FQRNT) (Grant No.: 199601).

References

[1] Erlandsson K. Tracer Kinetic Modeling: Basics and Concepts. Basic Sciences of Nuclear Medicine Berlin, Heidelberg: Springer, Berlin Heidelberg; 2010. p. 333–51. https://doi.org/10.1007/978-3-540-85962-8_16.
[2] Litton JE, Eriksson L. Transcutaneous measurement of the arterial input function in positron emission tomography. IEEE Trans Nucl Sci 1990;37(2):627–8.
[3] Watabe H, Miyake M, Narita Y, Nakamura T, Itoh M. Development of skin surface radiation detector system to monitor radioactivity in arterial blood along with positron emission tomography. IEEE Trans Nucl Sci 1995;42(4):1455–9. https://doi.org/10.1109/23.467729. URL: http://ieeexplore.ieee.org/lpdocs/epic03/wrapper.htm?arnumber=467729.
[4] Yamamoto S, Higashi T, Matsumoto K, Senda M. Preliminary study for the development of a tweezers-type coincidence detector for tumor detection. Nucl Instrum Methods Phys Res, Section A 2005;548(3):564–70. https://doi.org/10.1016/j.nima.2005.04.068.
[5] Villanueva A, Stoll S, Schlyer D, Shokouhi S, Vaska P, Woody C, et al. Spatial resolution of a noninvasive measurement of the arterial and venous input function using a wrist monitor. 2003 IEEE Nuclear Science Symposium. Conference Record (IEEE Cat. No.03CH37515) IEEE0-7803-8257-9; 2003. p. 2232–6. https://doi.org/10.1109/NSSMIC.2003.1352343. URL: http://ieeexplore.ieee.org/document/1352343/ papers2://publication/uuid/B017D670-72E1-45FF-AFF5-DB0D302C5A03.
[6] Kriplani A, Stoll SP, Southekal S, Schlyer DJ, Park SJ, Villanueva A, et al. Noninvasive high-resolution detection of the arterial and venous input function through a PET Wrist Scanner. IEEE Nucl Sci Symp Conf Record 2005;4(January):2240–4. https://doi.org/10.1109/NSSMIC.2005.1596780.
[7] Kriplani A, Schlyer D, Vaska P, Stoll S, Southekal S, Park S, et al. Non-invasive and selective measurement of the arterial input function using a PET Wrist Scanner. 2006 IEEE Nuclear Science Symposium Conference Record 2006. p. 3266–70. https://doi.org/10.1109/NSSMIC.2006.353705. URL:L http://ieeexplore.ieee.org/lpdocs/epic03/wrapper.htm?arnumber=4179747.
[8] Champion C, Le Loirec C. Positron follow-up in liquid water: II. Spatial and energetic study for the most important radioisotopes used in PET. Physics in Medicine and Biology 2007;52(22):6605–25. https://doi.org/10.1088/0031-9155/52/22/004. URL: http://stacks.iop.org/0031-9155/52/i=22/a=004?key=crossref.1daf17f2e1836466fb122a3a39da746d.
[9] Lee D, Kim JY, Kim HS, Lee KC, Lee SJ, Kwak HJ. Ultrasound evaluation of the radial artery for arterial catheterization in healthy anesthetized patients. J Clinical Monit Comput 2016;30(2):215–9. https://doi.org/10.1007/s10877-015-9704-9.
[10] Chichester DL, Watson SM, Johnson JT. Comparison of bcf-10, bcf-12, and bcf-20 scintillating fibers for use in a 1-dimensional linear sensor. IEEE Trans Nucl Sci 2013;60(5):4015–21. https://doi.org/10.1109/TNS.2013.2277799.
[11] Antonelli A, Antonelli M, Barbiellini G. Measurements of light yield, attenuation length and time response of long samples of blue scintillating fibers. Nucl Instrum Methods Phys Res, Section A 1996;370(2–3):367–71. https://doi.org/10.1016/0168-9002(95)00806-3.
[12] Archambault L, Arsenault J, Gingras L, Beddar AS, Roy R, Beaulieu L. Plastic scintillation dosimetry: optimal selection of scintillating fibers and scintillators. Med Phys 2005;32(7):2271–8. https://doi.org/10.1118/1.1943807.
[13] Knoll GF Radiation Detection and Measurement; vol. 3. 2000. ISBN 9780470131480. URL: http://www.wiley.com/WileyCDA/WileyTitle/productCd-EHEP001606, descCd-OVERVIEW.html. DOI: 10.1017/CBO9781107415324.004.
[14] Beddar S, Law S, Suchowerska N, Mackie TR. Plastic scintillation dosimetry: optimization of light collection efficiency. Phys Med Biol 2003;48(9):1141–52. https://doi.org/10.1088/0031-9155/48/9/305. URL: http://www.ncbi.nlm.nih.gov/pubmed/12765328.
[15] Chung M, Margulies S. Effects of stress and strain on scintillating and clear fibers. IEEE Tran Nucl Sci 1995;42(4):323–7.
[16] Hubbell J, Seltzer S. NIST: X-Ray Mass Attenuation Coefficients; 1996. URL: http://www.nist.gov/pml/data/xraycoef/.
[17] Berger MJ, Seltzer SM. Stopping powers and ranges of electrons and positrons. Vol NBSIR 82–2550; 1983; URL: http://adsabs.harvard.edu/abs/1982spre.reptQ.B.
[18] Taylor JR. An introduction to error analysis. Journal of the Acoustical Society of America 1997;101:330. https://doi.org/10.1121/1.418074. URL: http://link.aip.org/link/?JAS/101/1779/1&Agg=doi.
[19] Bushberg JT, Siebert JA, Leidholdt Jr EM, Boone JM. The Essential Physics of Medical Imaging. 2011. ISBN 978-0781780575. URL: https://books.google.ca/books?hl=fr&lr=&id=tqM8IG3f8bsC&oi=fnd&pg=PR1&dq=bushberg&ots=9njy4YjTnm&sig=-8aBt0FkFaLouBpKWDa7xYMGqQg#v=onepage&q=bushberg&f=false.
[20] National Nuclear Data Center. Nudat 2. URL: https://www.nndc.bnl.gov/nudat2/reCenter.jsp?z=6&n=5.
[21] Saint-Gobain. Scintillating Optical Fibers 2005;:1–6.
[22] Lo Presti D, Russo GV, Leonora E, Aiello S, Randazzo N, Sipala V, et al. Characterization technique of sub-millimeter scintillating fibers. IEEE Nucl Sci Symposium Conf Record 2012:2104–8. https://doi.org/10.1109/NSSMIC.2011.6154428.
[23] Davis A, Hink Binns PW, Epstein J, Connell J, Israel M, Klarmann J, et al. Scintillating optical fiber trajectory detector. Nucl Instrum Methods Phys Res 1989;276:347–58. URL: http://ac.els-cdn.com/0168900289906517/1-s2.0-0168900289906517-main.pdf?_tid=35bed14c-8287-11e7-a3f1-00000aab0f6b&acdnat=1502890477_db8ff4ac7dd347798985a8d8f32dbaa1 http://ac.els-cdn.com/0168900289906517/1-s2.0-0168900289906517-main.pdf?_tid=d6c58308-8285.

[24] Amos NA, Bross AD, Lundin MC. Optical attenuation length measurements of scintillating fibers. Nucl Inst Methods Phys Res, A 1990;297(3):396–403. https://doi.org/10.1016/0168-9002(90)91321-2.
[25] Hawkes CM, Kuhlen M, Milliken B, Stroynowski R, Wicklund E, Shimizu T, et al. Decay time and light yield measurements for plastic scintillating fibers. Nuclear Inst Methods Phys Res, A 1990;292(2):329–36. https://doi.org/10.1016/0168-9002(90)90388-M.
[26] Chung M, Margulies S. Aging studies on stressed and unstressed scintillating, wave-shifting, and clear fibers. SPOE 1995;2551:2–9.
[27] Shokouhi S, Stoll S, Villanueva A, Vaska P, Schlyer D, Woody C, et al. A Noninvasive LSO-APD Blood Radioactivity Monitor for PET Imaging Studies. IEEE Trans Nucl Sci 2003;50(5):1457–61. https://doi.org/10.1109/TNS.2003.817284. URL: http://ieeexplore.ieee.org/document/1236949/.
[28] Jelley JV. Cerenkov radiation and its applications. British Journal of Applied Physics 1955;6(7):227. https://doi.org/10.1088/0508-3443/6/7/301. URL: http://stacks.iop.org/0508-3443/6/i=7/a=301.
[29] Pain F, Laniece P, Mastrippolito R, Pinot L, Charon Y, Glatigny A, et al. SIC: An intracerebral radiosensitive probe for in vivo neuropharmacology investigations in small laboratory animals: prototype design, characterization, and in vivo evaluation. IEEE Trans Nucl Sci 2002;49(I(3)):822–6. https://doi.org/10.1109/TNS.2002.1039570.
[30] Goulet M, Gingras L, Beaulieu L. Real-time verification of multileaf collimator-driven radiotherapy using a novel optical attenuation-based fluence monitor. Med Phys 2011;38(3):1459. https://doi.org/10.1118/1.3549766.
[31] Beddar AS, Suchowerska N, Law SH. Plastic scintillation dosimetry for radiation therapy: minimizing capture of Cerenkov radiation noise. Phys Med Biol 2004;49(5):783–90. https://doi.org/10.1088/0031-9155/49/5/009. URL: http://stacks.iop.org/0031-9155/49/i=5/a=009?key=crossref.e42a9fefaac90643e35640846e4d246c.
[32] Beddar AS, Mackie TR, Attix FH. Water-equivalent plastic scintillation detectors for high-energy beam dosimetry: I. Physical characteristics and theoretical consideration. Phys Med Biol 1992;37(10):1883–900. https://doi.org/10.1088/0031-9155/37/10/006. URL: http://www.ncbi.nlm.nih.gov/pubmed/1438554.
[33] Beddar AS, Mackie TR, Attix FH. Cerenkov light generated in optical fibres and other light pipes irradiated by electron beams. Med Phys 1992;37(4):925–35. https://doi.org/10.1088/0031-9155/37/4/007. URL: http://iopscience.iop.org/0031-9155/37/4/007.
[34] Clift MA, Sutton RA, Webb DV. Dealing with Cerenkov radiation generated in organic scintillator dosimeters by bremsstrahlung beams. Phys Med Biol 2000;45(5):165–1182. https://doi.org/10.1088/0031-9155/45/5/307. URL: http://iopscience.iop.org/0031-9155/45/5/307 http://stacks.iop.org/0031-9155/45/i=5/a=307?key=crossref.b1e169e0989f8771febc505717d38f9b.